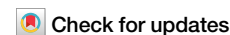


<https://doi.org/10.1038/s41612-025-01217-3>

Unraveling the interactions between tropical Indo-Pacific climate modes using a simple model framework

Hyo-Jin Park¹, Soon-Il An¹ ✉, Jae-Heung Park² & Chao Liu²

The dominant interannual climate phenomena are mainly observed in the tropical Indo-Pacific Ocean. While climate modes such as the El Niño–Southern Oscillation (ENSO), Indian Ocean Dipole (IOD), and Indian Ocean Basin (IOB) can develop through intrinsic basin dynamics, interactions between the Pacific Ocean (PO) and Indian Ocean (IO) significantly modulate their characteristics. Here, we quantified the impacts of tropical Indo-Pacific coupling using an extended nonlinear recharge oscillator model for ENSO that incorporates key tropical IO climate modes. Enabling the PO-to-IO effect increased the amplitudes of the IOD and IOB by 23% and 38%, respectively, and regulated IOB seasonality. Conversely, IO-to-PO connection increased ENSO peak variability by 5%, shortened its periodicity by 1 year, and more than doubled the frequency of extreme ENSO events when coupling strength was doubled. Over the past decade, strengthened Indo-Pacific interactions resulting from positive feedback between basins, have contributed to increased variability and occurrence of major climate modes.

The tropical Indo-Pacific region has the most dominant interannual modes, such as the El Niño–Southern Oscillation (ENSO), Indian Ocean Basin (IOB) mode, and Indian Ocean Dipole (IOD) mode. The ENSO is usually identified as the first empirical orthogonal function mode of tropical Pacific sea surface temperature anomalies (SSTAs), marked by interannual fluctuations between warm (El Niño) and cold (La Niña) phases over the tropical Pacific Ocean (PO)^{1,2}. The IOB and IOD, which are the first and second empirical orthogonal function modes of tropical IO SSTAs, feature a basin-wide pattern and zonal dipole structure of opposite SSTAs between the western IO and southeastern IO, respectively^{3–13}. These climate modes are closely linked not only through the oceanic pathway (i.e., Indonesian throughflow), but also via the “atmospheric bridge” of the Indo-Pacific Walker circulation^{4,14–16}. Given their wide-ranging impact and socioeconomic significance^{5,13,17–20}, it is crucial to understand how their interactions alter their characteristics that would appear in the absence of any interaction.

The ENSO typically develops during boreal summer, reaches its peak in winter, and dissipates by the following spring (hereafter, the seasons follow those in the Northern Hemisphere)^{1,2}. IO variability is strongly influenced by the ENSO^{15,16,21–25}. During the ENSO development phase, the IOD is often triggered in spring and co-evolves from summer to autumn. The IOD usually peaks in late fall and decays rapidly due to the seasonal reversal of the monsoonal winds^{6,7}. In winter, the IOD fades as its damping process dominates, but the continued influence of the ENSO causes

the development of the IOB through thermodynamic and dynamic processes^{14,26–28}. The dynamic process includes the effect of oceanic Rossby waves induced by the ENSO in the equatorial southeastern IO that propagates to the southwestern IO^{17,29}, whereas the thermodynamic process is dominated by the anomalous surface net heat flux^{4,30}. The IOB develops during the mature phase of the ENSO, peaks in early spring, and persists during summer²⁷. Specifically, El Niño (La Niña) is predominantly associated with a positive (negative) IOD and IOB. Consequently, the ENSO is recognized as the primary driver of IO climate variability.

Although IO variability is driven by the ENSO, both the IOD and IOB are recognized as intrinsic modes that can exist independently of the ENSO^{15,31–33} and, in turn, they can also influence²² the ENSO^{14,26,34}. Izumo et al. (2010)³⁴ demonstrated that IOD events can foster ENSO development in the following year by either accumulating or dispersing warm water in the western Pacific. Specifically, positive (negative) IOD events accompanied by equatorial easterly (westerly) winds lead to the dispersion (accumulation) of heat content in the tropical PO, thereby creating conditions favorable for La Niña (El Niño). Moreover, extreme IOD events co-evolving with the ENSO can contribute to ENSO development by modulating Walker circulation^{26,35,36}. In a series of hindcast experiments, the IO was found to contribute effectively to the development of extreme El Niño events³⁷. Thus, IOD events can facilitate the development of ENSO in the following year or positively modulate the development of the co-evolving ENSO. However, the IOB mode is known to contribute to the ENSO

¹Department of Atmospheric Sciences, Yonsei University, Seodaemun-gu, Seoul, Republic of Korea. ²School of Earth and Environmental Sciences, Seoul National University, Seoul, Republic of Korea. ✉ e-mail: sian@yonsei.ac.kr

lifetime. Because its peak phase occurs approximately one season later than the mature phase of the ENSO, it can significantly influence the decay process and transition of the ENSO by inducing equatorial surface wind anomalies in the tropical PO. Furthermore, the ENSO-driven IOB can act as a heat capacitor, and this oceanic heat memory affects the following Asian summer monsoon^{5,17} through atmospheric teleconnections. Thus, even after the ENSO dissipates, it can continuously influence the global climate through the ENSO-driven IOB mode. In summary, the IOD and IOB modes influence the ENSO differently, mainly because of their seasonal dependence.

Although the dominant interannual climate modes in the tropical Indo-Pacific basin are closely interconnected, most previous studies have mainly focused on one-way interactions using reanalysis data and climate model simulations. Only a few studies have quantitatively compared the characteristics of the Indo-Pacific climate modes by considering two-way interactions^{14,38,39}. Dommengot et al. (2006)³⁹ noted that signals outside the tropical Pacific basin can provide significant feedback to the ENSO, which also contributes significantly to ENSO predictability. In particular, Zhao et al. (2024)⁴⁰ highlighted the importance of inter-basin interactions in improving the ENSO forecast skill through an extended nonlinear recharge oscillator. This simple model framework enabled the isolation of interactions between climate modes through sensitivity experiments, thereby quantifying the role of each component in the interaction processes.

In this study, we developed a simple coupled model by integrating the climate modes of the tropical IO with the nonlinear recharge oscillator of the ENSO. A distinctive feature of this model compared to that of Zhao et al. (2024)⁴⁰ is its explicit separation of SSTAs in both the tropical western IO and tropical southeastern IO regions, where its variability is most pronounced, to represent IO climate modes. This approach was based on two key considerations. First, based on the observed SSTA standard deviation pattern (Supplementary Fig. 1a), variability was most pronounced in the tropical western and eastern IO regions within the entire IOB. Although these two regions are primarily linked through local processes, mainly via equatorial wind anomalies, they also exhibit independent characteristics. Second, the seasonal coupling between the ENSO and these two regions operates differently between the IOD and IOB^{41–44}. Wu et al. (2024)⁴¹ emphasized the role of the western IO in the rapid decay of El Niño events by

leading strong and earlier-peaking IOB events. By individually examining the interactions between the western and southeastern regions and their respective connections with the ENSO, this model effectively distinguishes each region's influence on the ENSO, while minimizing the overlapping effects between the IOD and IOB caused by regional redundancy. Accordingly, the IOD is defined as the difference between the western and southeastern indices, known as the dipole mode index, whereas the IOB mode is defined as the area-weighted average of these indices to characterize the uniform warming or cooling pattern of the entire IOB. This leads to the derivation of the IOB-like mode (IOB-M), which closely aligns with the traditional IOB index in terms of coherence, with a correlation of 0.92 (Supplementary Fig. 1b).

Results

Simulated characteristics of the Indo-Pacific climate modes using the extended Indo-Pacific recharge oscillator (XRO)

The XRO model effectively simulates key characteristics of the Indo-Pacific climate modes, including the seasonality of their standard deviation and interannual spectral peaks (refer to Methods) (Fig. 1). In our study, all variables refer to the XRO model results, and observed values will have “actual” prefixed to the variable name. The Niño3.4 amplitude (T_p) reaches its maximum in winter and minimum in summer (Fig. 1a). The thermocline depth anomalies averaged over the tropical equatorial Pacific basin (5S–5N; h_p) exhibit the strongest amplitude during spring owing to a 90-degree phase difference with the Niño3.4 index in the context of the recharge-discharge paradigm (Fig. 1b). The IOB-M index exhibits dominant variability from winter to summer and given its similar seasonality to the traditional IOB index, it is reasonable to define the IOB-M using only two regions (T_w and T_e) in the tropical IO instead of the entire basin (refer to Methods) (Fig. 1c). The IOD shows seasonal phase-locking characteristics, increasing in summer and peaking in autumn (Fig. 1d).

The XRO also simulated the periodic characteristics of each climate mode. The periodicity of the ENSO, IOB-M, and IOD exhibited dominant interannual peaks, with the IOD additionally featuring a quasi-biennial peak that was comparable to its dominant interannual peak (Fig. 1e–h). This quasi-biennial peak was strongly expressed at the eastern pole of the IOD (T_e), likely influenced by the ENSO C-mode dynamics²⁴ (Supplementary

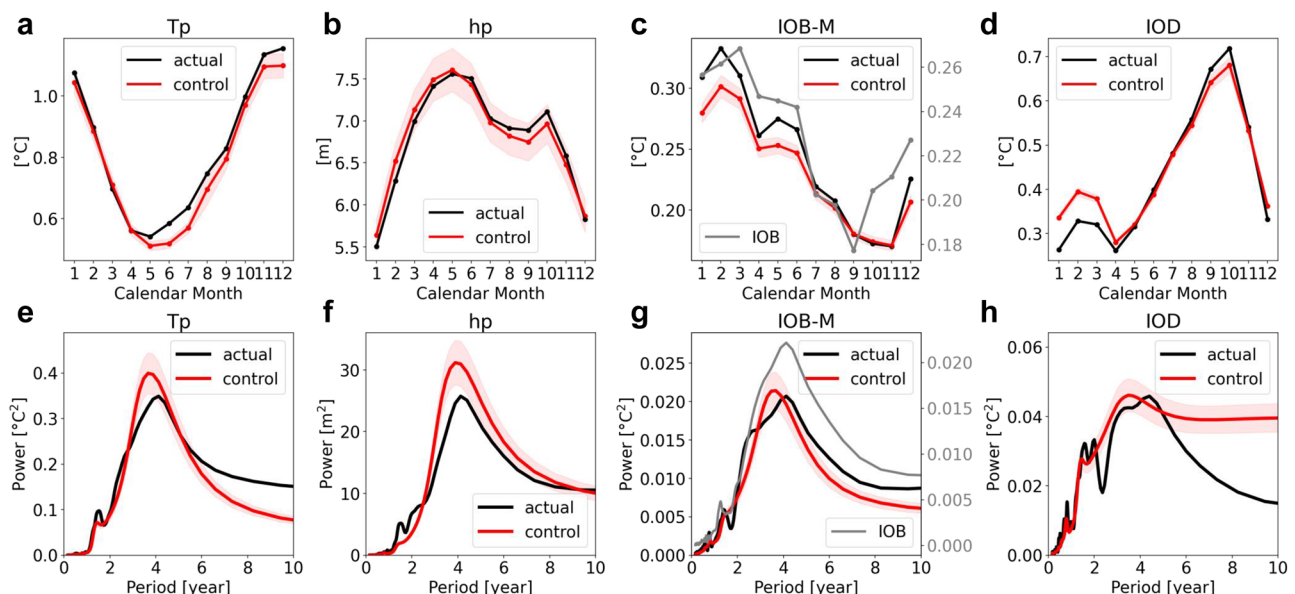


Fig. 1 | Model performance in simulating Indo-Pacific climate modes. Seasonal variations in the standard deviation of the (a) Niño3.4 (T_p), (b) tropical Pacific thermocline depth anomalies (h_p), (c) IOB-M, and (d) DMI from observations (black line) and model simulations (red line). The red shading represents the one-standard deviation inter-ensemble spread. **e–h** Show the power spectra of each index. The

gray lines in (c) and (g) represent the seasonal variations and power spectrum of the traditional IOB index, respectively. To enable a fair comparison of the power spectra between the actual and control experiment, 100 random segments of the control time series, each matching the length of the observed index, were extracted and averaged.

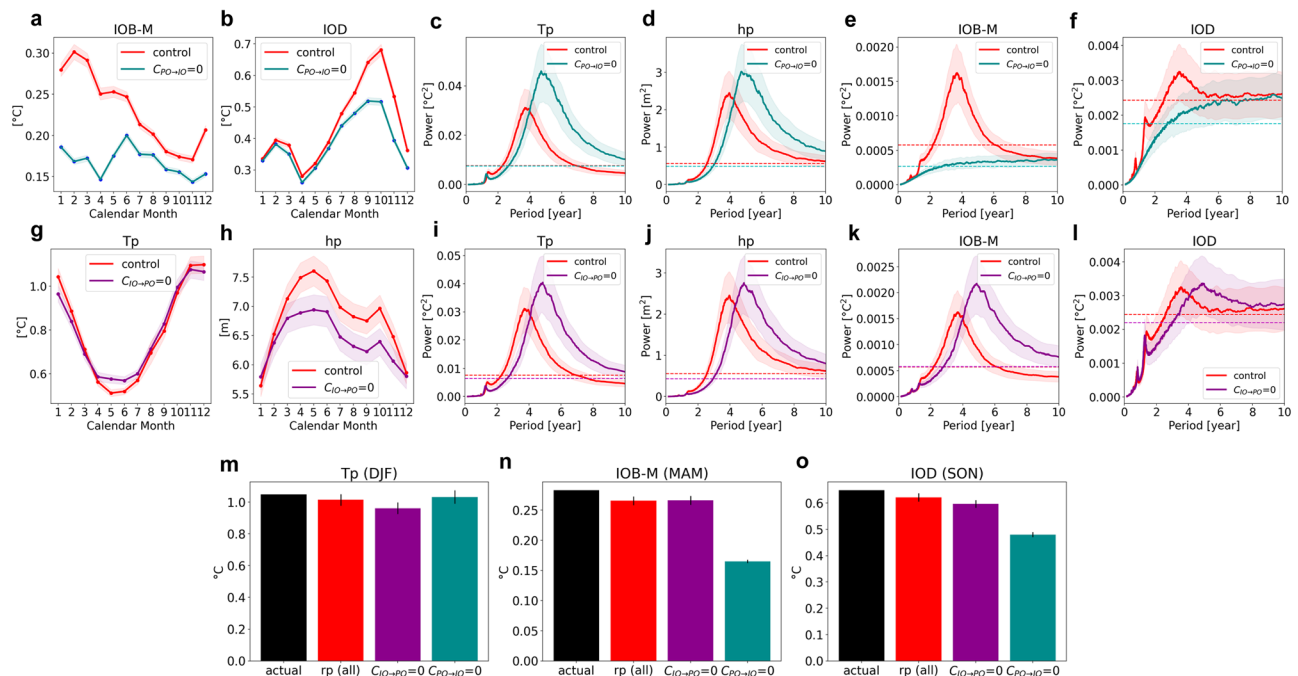


Fig. 2 | Effects of IO-PO coupling on each climate mode. Seasonal changes in the standard deviation of the (a) IOB-M and (b) DMI in the control experiment (red line) and in the sensitivity experiment when the Pacific Ocean (PO) coupling effect on the Indian Ocean (IO) is turned off (cyan line, $C_{PO \rightarrow IO} = 0$). Panels c–f as a, b, but for the power spectra of each index in the two simulations. Panels g–l as a–f, but for when IO coupling effect on the PO is turned off (cyan line, $C_{IO \rightarrow PO} = 0$). Shading

indicates a one-standard deviation inter-ensemble spread. The horizontal dotted line represents the significant level of each power spectrum. Panels show the standard deviations of the (m) Niño3.4, n IOB-M, and (o) DMI during their respective peak seasons: DJF, MAM, and SON. The black, red, magenta, and cyan bars represent the observation, control, $C_{IO \rightarrow PO} = 0$, and $C_{PO \rightarrow IO} = 0$ experiment, respectively.

Fig. 3d). Additionally, the model captured strong coupling between climate modes, as expressed by the simultaneous correlations between climate indices for each calendar month and their lead-lag relationships (Supplementary Fig. 4). The correlation between the ENSO and IOB-M peaked in late winter, with a coefficient of 0.8, whereas its strongest association with the IOD occurred in late autumn, with a coefficient of 0.67. The XRO model broadly captured the observed autocorrelation of each climate mode and their lead-lag relationship. By capturing the unique characteristics of each mode and the coupling structures between them, the model provides a robust framework for quantitatively assessing the impact of coupling in each basin on the various characteristics of the climate modes.

Coupling effect of the PO on the variability and periodicity of Indian Ocean climate modes (PO-to-IO)

To examine the role of coupling effects, we conducted several decoupled experiments and compared them with a control experiment (refer to “Methods”). This allowed us to identify the individual contributions of the IO and PO coupling effects on the climate modes.

When the effect of the PO on the IO was switched off, interannual variability of both IOB-M and IOD modes substantially decreased (Fig. 2a, b, e, f). The IOB-M was largely suppressed from winter to spring, whereas the IOD amplitude was mainly affected by the ENSO during fall. In particular, during the peak seasons, the standard deviations of the IOB-M and IOD were reduced by approximately 38% and 23%, respectively (Fig. 2a, b, n, o). Without the PO-to-IO effect, the dominant biennial and interannual peaks of IO variability were suppressed, and their corresponding spectra resembled a red noise spectrum (Fig. 2e, f). This result suggests that the effect of the PO on the IO is a key driver of IO interannual variability. Furthermore, this supports the argument of Stuecker et al. (2017)²⁴ that the quasi-biennial peak of the IOD is driven by the ENSO C-mode dynamics.

Interestingly, despite the presence of IO coupling, there were notable changes in ENSO variability and periodicity (Fig. 2c, d and Supplementary Fig. 5a, b). Although the shift in ENSO periodicity can be largely attributed

to weakened IO variability, the change in ENSO amplitude cannot be explained by IO variability alone. Rather, the removal of PO forcing modified the interactive dynamics between the IO and PO systems, leading to nonlinear changes in the ENSO system. This suggests that the impact of the IO on the ENSO depends not only on its intrinsic variability, but also on its coupling with, and feedback from, the PO. The distinct roles of IO-PO coupling are further elaborated in the varying coupling experiment presented later.

To identify which IO region was more sensitive to the ENSO coupling effect, we conducted additional sensitivity experiments by selectively decoupling the coupling effect of the PO on each IO region. When the coupling effect of the PO on the western and eastern IO was independently turned off, the standard deviation of the IOB-M decreased by 34% and 15%, respectively, whereas that of the IOD decreased by 13% and 15%, respectively (Supplementary Fig. 6a, b, n, o). These results indicate that the influence of the ENSO on the IOB-M is stronger through the western IO⁴⁵, whereas the difference in its influence on each area of the IOD is somewhat indistinguishable, possibly because of a strong dynamic connection between the western and southeastern tropical IO.

Coupling effect of the IO on the variability and periodicity of ENSO (IO-to-PO)

When the effect of the IO on the PO was turned off, ENSO variability and periodicity also changed. The ENSO variance measured by T_p decreased by approximately 5% during the peak season but increased in summer (Fig. 2g, h, m); thus, the seasonality of the ENSO variance weakened. The ENSO period was approximately 1 year longer, and the periodicities of the IOB-M and IOD were also approximately 1 year longer. Changes in the IOB-M and IOD dominant periods were related to changes in the ENSO dominant period. These results align with those of previous studies using coupled GCMs and empirical models, which found that IO variability, particularly the IOD and IOB, acts as a negative feedback to the ENSO, accelerating its phase transition and shortening its cycle (Fig. 2i–m)^{14,22,46}.

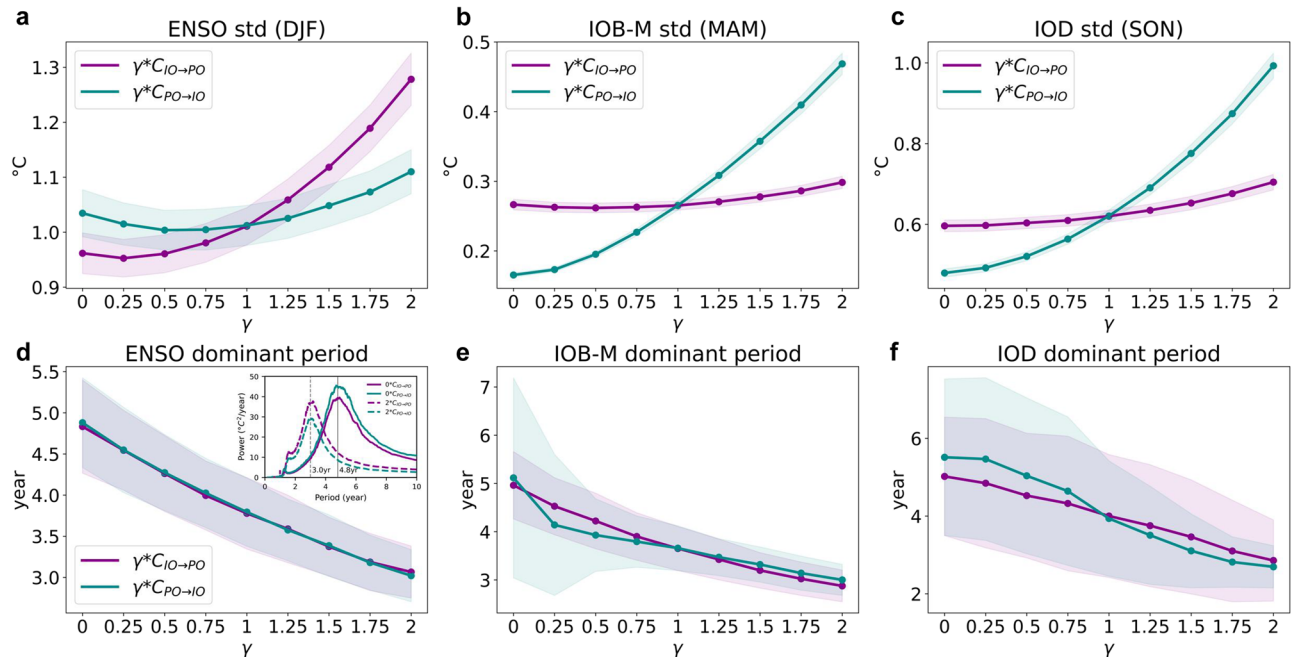


Fig. 3 | Variability and periodicity under varying coupling strengths. Dependence of the standard deviation of the (a) ENSO, (b) IOB-M, and (c) IOD on the coupling strength adjusted by multiplying the coupling coefficient (γ) with $C_{IO \rightarrow PO}$ (magenta line) and $C_{PO \rightarrow IO}$ (cyan line). Panels illustrate the dependence of the periodicity of

the (d) ENSO, (e) IOB-M, and (f) IOD on varying coupling strengths. The inset in (d) presents the power spectra for each experiment at $\gamma = 0$ and $\gamma = 2$, highlighting the shift in the dominant periodicity of ENSO. Shading indicates a one-standard deviation of 1000 ensembles.

Because the western and eastern poles of the IOD interact differently with the ENSO, we identified the distinct roles of each region. Although the two poles are connected by IO internal circulation, each pole's impact on the PO highlights its independent influence on the ENSO by turning off each pole. The coupling effect of the western IO on the PO showed little impact, whereas the coupling effect of the eastern IO reduced the ENSO variance in winter by 7.5% compared with the control experiment (Supplementary Fig. 6g,h,m). This indicated that the eastern IO has a more dominant influence on the PO than the western IO. During the ENSO period, both regions contributed similarly to the shortening of its cycle.

Additionally, we conducted experiments to distinguish the effects of the IOB-M and IOD, represented by a combination of T_w and T_e , based on model equations, to better understand their respective roles in ENSO variability and periodicity (see “Methods”). The results revealed that IOD played a more significant role in modulating ENSO peak variability during DJF season, while both the IOB-M and IOD contributed to the variability of the thermocline depth anomalies in the Pacific Ocean (Supplementary Fig. 7).

To obtain a more comprehensive view of the dependence of the IO-PO climate mode characteristics on inter-basin coupling, we performed idealized sensitivity experiments with varying coupling strengths by gradually adjusting the amplification factor of the annual cycle of the coupling strength from 0 to 2 (see Methods). As PO coupling strengthened, both the IOD variance in fall and the IOB-M variance in spring increased (Fig. 3b, c). Similarly, stronger IO coupling amplified the ENSO variance in winter (Fig. 3a). Here, we found that the relationship between coupling strength and climate mode variability is not simply linear, but rather quadratic, with a greater increase in variability as the coupling strength increases, which is likely due to the interactive enhancement between the IO and PO climate modes. Specifically, ENSO variance increased not only when the PO-to-IO coupling was removed, as shown in the previous results, but also when the coupling strength was enhanced, suggesting nonlinear and potentially bidirectional sensitivity. Furthermore, when the IO-to-PO coupling was weakened, the variability did not decrease linearly, which coupling strength 0 ($\gamma = 0$) was bigger than at ($\gamma = 0.25$), indicating a non-monotonic, nonlinear response.

Interestingly, as the coupling strength increased, the dominant periodicity of all climate modes linearly decreased. This suggests that stronger coupling enhances the frequency of variability, potentially shortening the lead-time for skillful predictions. Furthermore, as IOB-M coupling to the ENSO increased, ENSO variability exponentially increased, whereas the change in IOD coupling modulate ENSO variability linearly (Supplementary Fig. 8). This suggests that the nonlinear response of ENSO to Indian Ocean coupling is primarily due to the IOB-M. Interesting point is that under weaker coupling conditions, the IOD exerts a stronger influence on ENSO compared to IOB-M. However, as the IO-to-PO coupling strength increases, the influence of IOB-M on ENSO grows exponentially and eventually dominates. Additionally, IOB-M variability was more sensitive to ENSO coupling with the western IO, whereas IOD variability was more sensitive to ENSO coupling with the eastern IO under sufficiently strong coupling (Supplementary Fig. 9).

Influence of IO coupling on the ENSO frequency

In the previous section, we demonstrated how the coupling between the IO and PO influences both the variability and periodicity of the Indo-Pacific climate modes. Building on these findings, we now explore the specific impact of the IO coupling effect on the ENSO frequency, further highlighting its role in shaping ENSO characteristics. Considering that IO coupling to the PO strengthens ENSO variability and shortens its period, we examined the occurrence frequency of different ENSO types, i.e., single-year ENSO, multi-year ENSO, and extreme ENSO, with respect to the IO coupling strength. As the IO-to-PO coupling strengthened, the frequencies of both El Niño and La Niña increased nonlinearly, with a faster ENSO cycle (Fig. 4a, e). The rate of increase in the ENSO frequency against a unit of coupling strength becomes significantly larger when the coupling factor exceeds 1. Under weak coupling condition, the ENSO frequency has increased as IO-to-PO coupling becomes weaker. However, changes in the PO-to-IO coupling did not significantly modify the ENSO frequency (Fig. 4a, e). Here, the increase in the ENSO frequency was related to a higher occurrence rate of single-year ENSO events, driven by a stronger IOB effect. Because the IOB assists in ENSO termination, more frequent single-year ENSO events with shorter cycles can occur (Fig. 4b, f). The frequency of

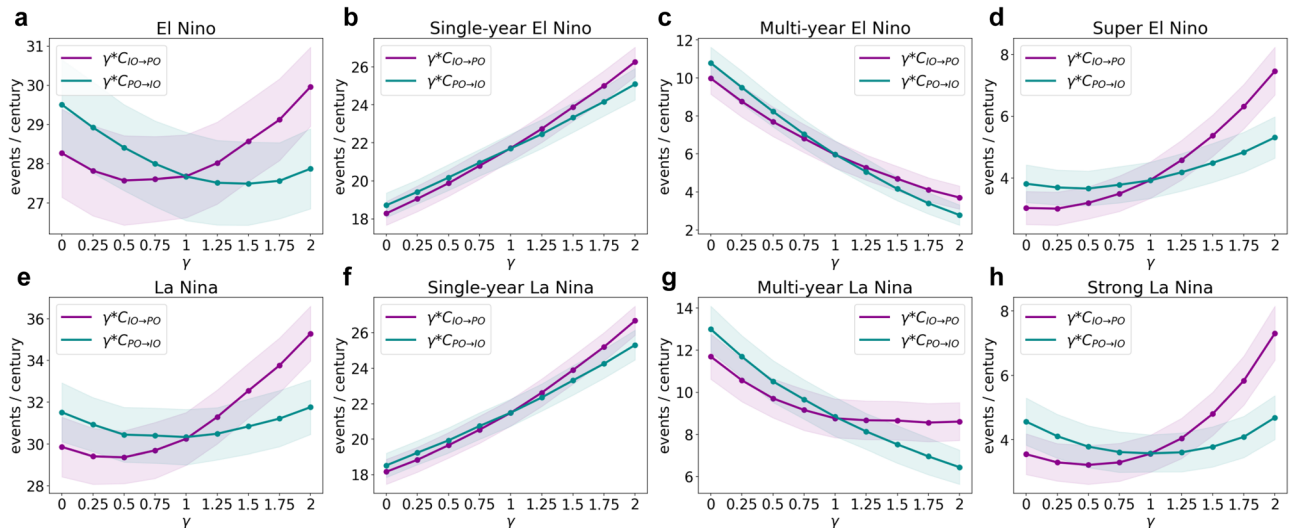


Fig. 4 | Frequency of the ENSO under varying coupling strengths. Dependence of the frequency of **a** El Niño, **b** Single-year El Niño, **c** Multi-year El Niño, **d** Extreme El Niño, **e** La Niña, **f** Single-year La Niña, **g** Multi-year La Niña, and **(h)** Strong La Niña

on the coupling strength, determined by multiplying the coupling coefficient (γ) with $C_{IO \rightarrow PO}$ (magenta line) and $C_{PO \rightarrow IO}$ (cyan line). Shading indicates a one-standard deviation of 1000 ensembles.

ENSO transitions led by IOB-M events also increased, with a stronger IO coupling effect (Supplementary Fig. 10a, d).

Conversely, the frequency of multi-year ENSO events decreased as IO coupling strengthened. Specifically, the frequency of multi-El Niño events showed a monotonic decrease with increasing coupling strength, whereas that of multi-La Niña events exhibited nonlinear responses with no significant changes at high coupling strengths. This indicates an asymmetric impact of IO coupling on El Niño and La Niña frequencies, likely originating from the inherent asymmetry in ENSO patterns⁴⁷. Moreover, a stronger IO-to-PO effect led to a nonlinear increase in the frequency of both extreme El Niño and La Niña events, highlighting the role of IO in amplifying the ENSO variability during its peak season (Fig. 4d and h). This amplification occurs by increasing ENSO amplitude, thereby elevating the likelihood of extreme ENSO events. Notably, this effect was primarily transmitted through the IOB-M rather than the IOD (Supplementary Fig. 11). This nonlinear feature in the IOB's impact on ENSO stems from its dynamical interaction with ENSO. The IOB is known to contribute to the rapid decay of ENSO events and/or facilitate phase transitions. To investigate this relationship further, we analyzed how the frequency with which the IOB leads the neutral or opposite-phase ENSO events responds to changes in IO-to-PO coupling strength. As shown in Supplementary Fig. 12, the frequency of IOB events leading El Niño or La Niña increases approximately linearly with enhanced coupling. In contrast, the frequency of IOB events preceding neutral ENSO conditions exhibit a nonlinear response.

These findings suggest that under weak coupling, increased IO-to-PO coupling primarily facilitates the decay of ENSO events back to neutral conditions, thereby reducing the overall ENSO amplitude and frequency. In contrast, under stronger coupling, positive (negative) IOB anomalies not only accelerate the decay of El Niño (La Niña) but also initiate phase transitions toward La Niña (El Niño), thereby amplifying both the amplitude and frequency of ENSO events.

However, in contrast to the ENSO, the frequencies of the IOD and IOB-M events remained largely unaffected by changes in the strength of the PO-to-IO effect. However, as the PO-to-IO effect became stronger, the co-occurrence ratio of the IOD with the ENSO increased, whereas the fraction of independent IOD events decreased (Supplementary Fig. 10b, c, e, f).

Independent role of IO variability on the ENSO

While previous results suggest that the periodicity of IO variability is primarily driven by the ENSO, it remains unclear how independently occurring IOD or IOB events—arising from local feedback and stochastic forcing—might

influence the ENSO. To address this, we isolated the PO-to-IO and IO-to-PO effects by comparing a control experiment with a decoupled experiment. First, we confirmed that our model effectively simulated the lead-lag relationship between the IO climate modes and ENSO (Fig. 5a, b, e, f).

The IOD, particularly during its life cycle from June to December, exhibited a strong simultaneous positive correlation with a maximum correlation coefficient of 0.66 when the IOD leads ENSO by one month. However, as the IOD either dissipated or transitioned, starting in January of the following year, its simultaneous correlation with the ENSO became negative, indicating a loss of intrinsic characteristics. When the ENSO led, the positive lead correlation strengthened within a season, particularly from June onwards. As the IOD phase shifted, the correlation sign reversed. In contrast, when the IOD led, the strongest positive lagged correlation appeared 2–3 months after the IOD reached its peak in autumn. However, after 8 months, as the ENSO began to shift phase, the correlation between the IOD and ENSO became negative (Fig. 5a, b).

Decoupling the PO-to-IO effect dramatically weakened the positive correlation, making it insignificant, suggesting that the ENSO tends to lead the IOD in cases of simultaneous development. Instead, a weak negative leading correlation with the IOD remained (Fig. 5c). The IOD could lead to the ENSO for 8 to 15 months during its active season, but the removal of the IO-to-PO effect resulted in a longer persistence of the positive relationship (Fig. 5d). Consequently, the leading negative correlations after 1 year of the IOD disappeared under this setting (Fig. 5d).

The IOB-M, during its life cycle from December to April, exhibited a strong positive simultaneous correlation with the ENSO, which persisted until late spring of the following year (Fig. 5e, f). The leading effect of the ENSO on the IOB-M maintained a robust positive correlation for up to a year. However, when the IOB-M led the ENSO, a pattern similar to that of the IOD emerged. As the ENSO started to shift phase, the correlation sign reversed accordingly. Despite this reversal, the correlation remained significant and large, persisting for approximately 1 year.

When the PO-to-IO coupling was shut down, the positive correlation was significantly weakened, leaving only a significant negative correlation when the IOB-M led to the ENSO (Fig. 5g). The IOB-M could lead the ENSO negatively from January to August, suggesting a longer influence window than the IOD. Conversely, decoupling IO-to-PO resulted in a longer persistence of the positive relationship, eliminating the one-year leading negative correlations observed for both the IOD and IOB-M (Fig. 5h). However, the negative leading correlation of the IOB-M with the ENSO over a one-year timescale remained under the IO-to-PO decoupling

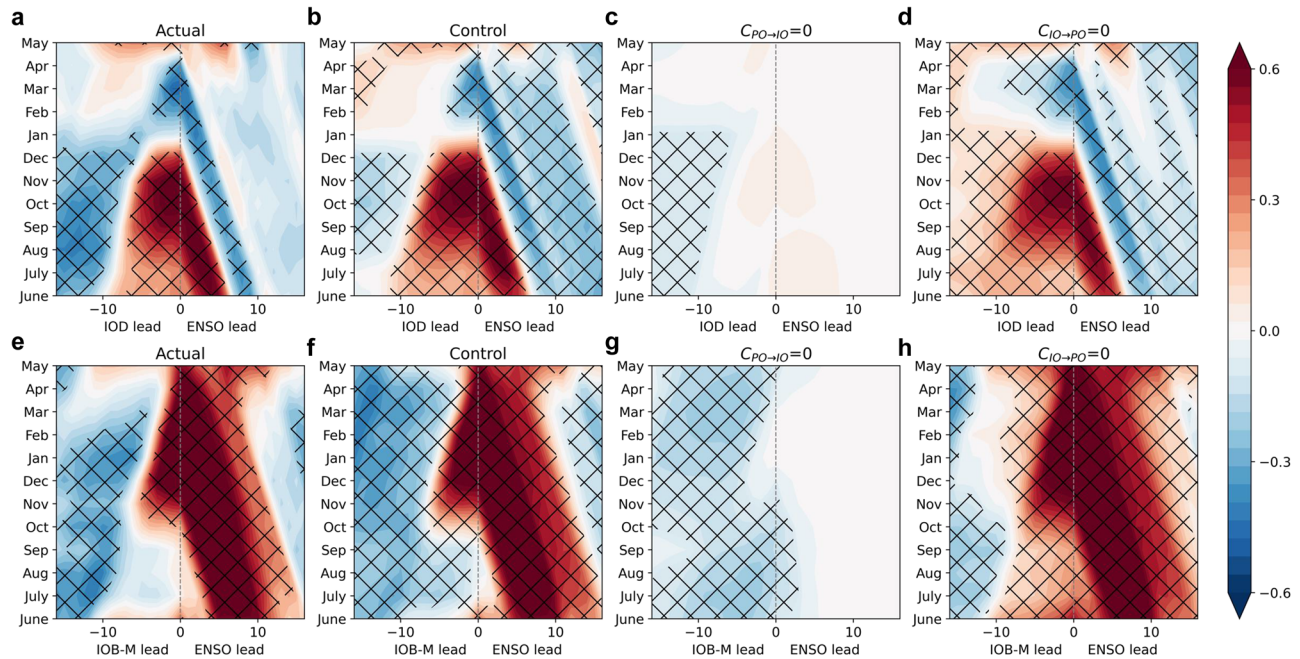


Fig. 5 | Lead-Lag relationship between IO variability and the ENSO. Lead-lag correlation between the IOD and ENSO indices for (a) the actual observation, (b) the control experiment, (c) $C_{PO \rightarrow IO} = 0$, and (d) $C_{IO \rightarrow PO} = 0$. The x-axis represents the lead month, where negative values indicate the IOD-leading ENSO and positive

values indicate the ENSO-leading IOD. The y-axis spans from June to May. Hatching indicates a 90% confidence level based on Student's *t* test. Panel e–h show the same analysis as a–d, but for the relationship between the IOB-M and ENSO indices.

experiment, implying that this feature is primarily driven by the auto-correlation of the ENSO (Fig. 5h). This finding highlights the distinct roles of the IOD and IOB-M in leading the opposite phase of the ENSO in the following year, as demonstrated by their lead-lag relationships. This suggests that IO variability can influence the ENSO beyond its direct coupling with it.

Decadal changes in the coupling strength and climate modes

Because the coupling strength between the IO and PO changes over time, we illustrated a regime diagram depicting the variability and dominant periods of the three climate modes as a function of the IO-to-PO and PO-to-IO coupling strengths (Fig. 6). Subsequently, we compared these results with the actual decadal changes in the coupling strength and characteristics of each climate mode using a 30-year moving window. As the strength of the IO-to-PO effect increased, ENSO amplitude increased significantly (Fig. 6a). However, the role of the PO-to-IO effect on ENSO amplitude became notable only when both the PO-to-IO and IO-to-PO effects were strong. In contrast, the amplitudes of the IOB-M and IOD were strongly influenced by the PO-to-IO effect (Fig. 6b, c). The amplitudes of IOD and IOB-M were influenced by the IO-to-PO effect only under the higher-strength regime of both the PO-to-IO and IO-to-PO effects.

Regarding the dominant periods of the climate modes, the ENSO period shortened as both coupling effects increased. However, both IOD and IOB-M periodicities exhibited greater sensitivity to changes in the PO-to-IO coupling strength in the low range (0–0.5), but their sensitivities were comparable to that of the ENSO under sufficiently strong PO-to-IO coupling.

The actual decadal changes in both coupling strengths revealed a strengthening trend in recent decades (gray arrow in Fig. 6a). These coupling strengths (denoted as $C_{PO \rightarrow IO}$ and $C_{IO \rightarrow PO}$) were estimated as an equally weighted average of the interactions between the PO variables (T_p , h_p) and IO variables (T_w , T_e) over a 30-year moving window. There values are interpreted as relative strengths normalized by the full period estimates. For example, $C_{Tp \rightarrow Tw}$ represents the regression coefficient between the monthly coupling parameter c_{pwil} , estimated in each 30-year moving window, and its corresponding full period estimate over 1958–2023. Then, $C_{PO \rightarrow IO}$ is computed as the average of four such regressions: $C_{Tp \rightarrow Tw}$, $C_{Tp \rightarrow Te}$, $C_{hp \rightarrow Tw}$, and $C_{hp \rightarrow Te}$. Similarly, $C_{IO \rightarrow PO}$ is defined in the same

manner but in the reverse direction. Both coupling strengths have exhibited a steadily increasing trend since the 1980s (Supplementary Fig. 13). The decadal variability of the three climate modes simulated by the XRO model (Supplementary Fig. 14) is shown in Fig. 6. It shows an increasing trend in variability and a decreasing trend in the dominant ENSO, IOB, and IOD periods. While the decadal changes in IOD and IOB-M amplitudes closely followed the decadal variation in the PO-to-IO effect, the ENSO did not exhibit perfect correspondence. This suggests that inter-basin coupling alone cannot fully explain the decadal changes in ENSO, underscoring the critical contribution of intrinsic ENSO dynamics. Nevertheless, the enhanced IO-to-PO effect during recent decades can account for up to 21% of the increase in ENSO variance, highlighting a non-negligible contribution of Indo-Pacific coupling to ENSO intensification.

A fixed coupling experiment was conducted to assess whether the recent intensification in variability and changes in their dominant periods were due to the increased coupling strength between the IO-PO basins. In this experiment, the coupling strength was held constant using parameters fitted across the entire period, whereas the local parameters varied over time. The index was reconstructed using a 30-year moving window (Supplementary Fig. 15). In the fixed coupling experiment, the standard deviations of ENSO and IOD decreased after the mid-1980s compared with the control experiment. Although the IOB-M showed an increasing trend during the earlier period, it exhibited a decreasing trend after the mid-1980s. Moreover, shortening of the dominant period was not observed in the fixed coupling experiments. Consequently, as shown in the regime diagram, increasing coupling strengths have contributed to the intensification of Indo-Pacific variability in recent decades.

Discussion

The tropical Indo-Pacific region is the origin of several dominant climate modes that significantly influence global climate. Recent studies, including Zhao et al. (2024)⁴⁰, have emphasized the importance of inter-basin precursors—extending beyond the PO to include variability in other basins—in enhancing ENSO predictability. Building on this framework, the present study further investigates Indo-Pacific interactions using a non-linear recharge oscillator coupled with the tropical IO, based on

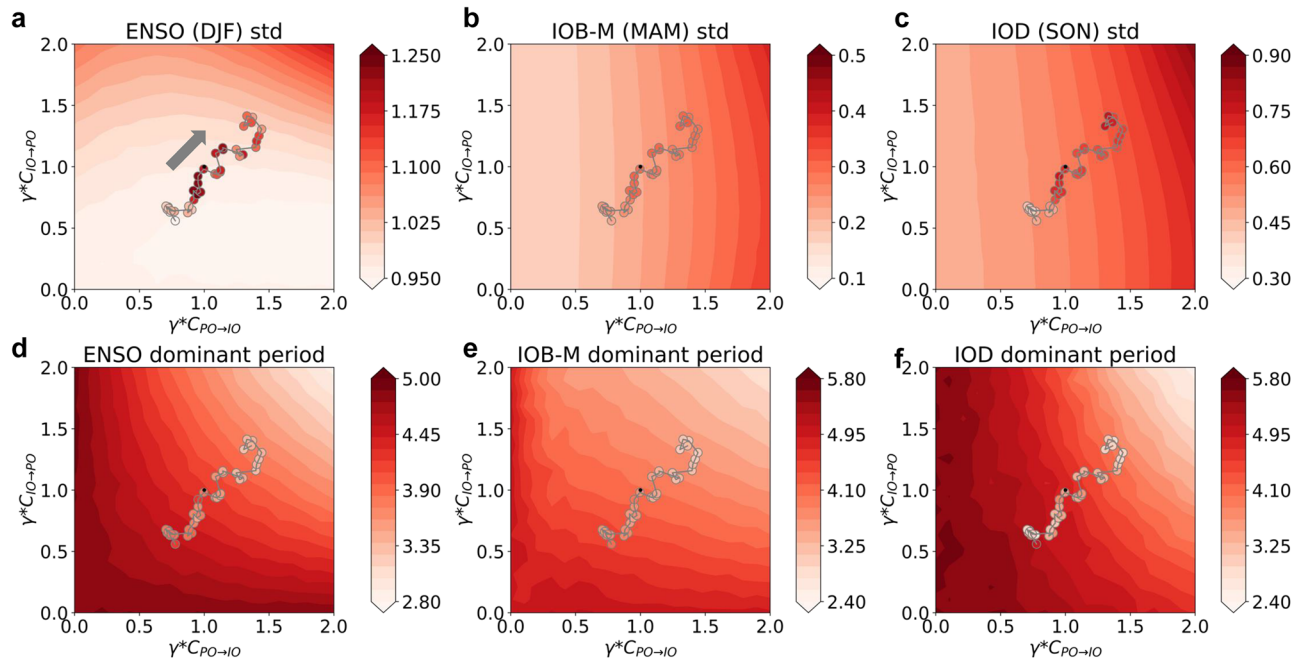


Fig. 6 | Sensitivity of Indo-Pacific climate modes to coupling strength between the two basins. Regime diagram of standard deviations of the **a** ENSO, **b** IOB-M, and **c** IOD for each peak season with respect to the PO-IO coupling (x-axis) and the IO-PO coupling (y-axis) (contour). The decadal changes in coupling strength, calculated using a 30-year moving window, are indicated as scatter points within the

contour. The colors of the scatter plots represent the simulated decadal variability of the climate modes from the time-varying coupling experiments. Panels **d–f** show the dominant periods of the three climate modes, with the other details remaining the same as those in **a–c**. The gray arrow in **a** indicates the progression of time.

observational reanalysis data. A key contribution of this study lies in its quantitative assessment of two-way inter-basin coupling, with a particular focus on the feedback nature of these interactions. Specifically, our results show that PO-to-IO coupling plays a dominant role in driving interannual variability in the Indian Ocean, while strengthening of IO-to-PO coupling leads to amplified ENSO variability and a shorter periodicity, thereby increasing the frequency of both extreme and single-year ENSO events. These bidirectional coupling effects mutually reinforce each other, revealing the nonlinear responses of each climate mode as the coupling becomes stronger.

Furthermore, we identify decadal changes in coupling strength, highlighting the evolving nature of Indo-Pacific interactions and their contribution to recent climate variability. The recent intensification of variability and shortening of the dominant periods of the three climate modes are likely related to the stronger coupling observed in recent decades. In particular, the characteristics of Indo-Pacific climate modes have undergone significant changes since the 1970s^{23,28,48–53}, including an increase in the ENSO amplitude^{54,55}. Consistent with this, the intensification of the IOB and IOD has also been observed in historical records^{50,56}. Several studies have emphasized the critical role of inter-basin interactions, particularly the stronger influence of the ENSO on the IOD, which has led to an increase in IOD amplitude since the 1970s^{23,28}. According to previous studies, the ENSO-to-IOB coupling is influenced by the Atlantic Multidecadal Oscillation⁵⁷, while the ENSO-to-IOB coupling is modulated by the Interdecadal Pacific Oscillation⁵⁸. Although the impact of the ENSO on IO variability has been extensively explored, decadal changes in the influence of IO on the ENSO remain largely unexamined. Therefore, this study advances our understanding of Indo-Pacific climate mode interactions by demonstrating that decadal variations in the influence of IO on the ENSO have also intensified over time, particularly in the context of two-way interactions between the two basins.

These observed changes are also relevant in the context of global warming. Although there is evidence that anthropogenic forcing can modify ENSO dynamics—through processes such as the weakening of tropical Pacific upwelling and changes in thermocline structure⁵⁹—the projected

behavior of inter-basin coupling remains uncertain, with no clear consensus among models. Given this uncertainty, our conceptual modeling framework, which explicitly links coupling strength to variability and frequency of ENSO and IO modes, offers valuable insights into how changes in Indian Ocean may influence Pacific variability under future climate changes.

The steady increase in the Indo-Pacific coupling strength in recent decades appears to be associated with mean state changes, likely driven by decadal-to-interdecadal variability or long-term trends related to global warming (Supplementary Fig. 13). We suggest that the strengthening influence of the Indian Ocean on ENSO may be related to mean state changes in the Pacific, which may enhance the Pacific Ocean's sensitivity to IO impact. Notably, during the recent decades of increased IO-to-PO coupling, the mean thermocline depth of Pacific Ocean has shoaled significantly (trend: -0.16 m year $^{-1}$, p value < 0.0001). This shoaling implies that Pacific SST change has become more sensitive to thermocline depth changes induced by the Indian Ocean's teleconnection. Such changes are consistent with the Pacific Climate Change pattern shown in a previous study⁶⁰.

A comprehensive understanding of Indo-Pacific coupling effects in the present climate is crucial for improving climate model performance and enhancing the reliability of future projections. However, biases in climate models and significant uncertainties remain major challenges for obtaining accurate projections. Additionally, current climate models tend to over-emphasize the influence of the PO, while underrepresenting the role of other basins in modulating Pacific variability. To address these limitations, efforts should be focused on understanding the role of inter-basin coupling effects in present-day climates and how they relate to changes in the mean state. This study underscores the need for further investigation of current climate model simulations using a process-based approach, as well as the development of more advanced methodologies for improving future projections based on these findings.

Methods

XRO model

To investigate the coupling effect between the tropical IO and PO, an XRO model was utilized. This model features a nonlinear recharge oscillator

model for the ENSO coupled with stochastic deterministic models for IO regions.

$$\frac{d}{dt} \begin{pmatrix} X_{PO} \\ X_{IO} \end{pmatrix} = L \cdot \begin{pmatrix} X_{PO} \\ X_{IO} \end{pmatrix} + \begin{pmatrix} N_{PO} \\ 0 \end{pmatrix} + \sigma_{\xi} \xi \quad (1)$$

$$\frac{d\xi}{dt} = -r_{\xi} \xi + w(t) \quad (2)$$

where $X_{PO} = [T_p, h_p]$ and $X_{IO} = [T_w, T_e]$ are the state vectors of the ENSO and IO, respectively. X_{PO} contains SSTAs averaged over the Niño3.4 region (170°W–120°W and 5°S–5°N) and thermocline depth anomalies averaged over the equatorial Pacific (120°E–80°W and 5°S–5°N). The thermocline depth is defined as the depth of the 20 °C isotherm. For X_{IO} , we considered SSTAs averaged over the western IO (50°E–70°E and 10°S–10°N) and southeastern IO (90°E–110°E and 10°S–EQ).

The state vectors are dynamically driven by linear dynamics (L), nonlinear dynamics (N), and stochastic (ξ) parts. The linear dynamics contains the local damping and coupling coefficients, as follows:

$$L = \begin{pmatrix} L_{PO} & C_{IO \rightarrow PO} \\ C_{PO \rightarrow IO} & L_{IO} \end{pmatrix} \quad (3)$$

where L_{PO} indicates the ENSO internal recharge-discharge dynamics and L_{IO} represents the internal processes of the tropical IO. $C_{IO \rightarrow PO}$ is the impact of IO on the ENSO. This includes the effects of the atmospheric and oceanic pathways. The IO can influence the ENSO SST or thermocline, either by modulating winds through the Walker Circulation or by transporting heat through the Indonesian Throughflow. $C_{PO \rightarrow IO}$ is the impact of the ENSO on the IO, which contains the effect of the PO to IO SST in a similar way. Note that in this conceptual model, coupled dynamics are formulated as linear and time-invariant for simplicity. Accordingly, linear connections between two basins—such as those mediated by wind bursts and Walker circulation anomalies—are incorporated into the coupling parameter as an averaged influence of inter-basin teleconnections. Meanwhile, to explore the influence of time-varying coupling, we performed parameter fitting using a 30-year moving window.

To simulate realistic ENSO characteristics, we included nonlinear dynamics related to ENSO asymmetry and quadratic nonlinearities $b_1 T_p^2 + b_2 T_p h_p$ in N_{PO} ^{61–63}. However, nonlinearities were not observed in the IO. The detailed equations for the model are provided in the Supplementary Text 1.

Lastly, stochastic forcing (ξ) including synoptic eddies and high frequency is described as red noise with decorrelation time scales of r_{ξ} and amplitudes of σ_{ξ} , respectively. The r_{ξ} is calculated by lag-1 autocorrelation of the residual of the fitting. This formulation does not account for multiplicative noise effects arising from nonlinear processes, such as enhanced westerly wind bursts associated with background SST change and Madden-Julian Oscillation modulated by the Indian Ocean, and these influences are therefore beyond the scope of this study. For parameter fitting of this model, least-squares fitting with the forward Euler method was applied to the indices to compute the parameters for each calendar month. The fitted parameters are shown in Supplementary Fig. 2.

The observational SST and depth of 20 °C isotherm during 1958–2023 were derived from the Ocean Reanalysis System5 (ORAS5) global ocean reanalysis⁶⁴. SSTAs were calculated by removing the monthly climatology for the entire period and were quadratically detrended to remove the observed long-term trends.

Model simulations

To assess the simulation skill of the XRO model, we conducted stochastic simulations using parameters estimated from the ORAS5 reanalysis for the period of 1958–2023. A control experiment was performed by integrating the model equations with a timestep of 0.1 month for 5000 years, repeated 1000 times with different random noises to generate ensemble members. To

ensure scale consistency at a fine time resolution, the local damping coefficients, T_w and T_e , were slightly adjusted. This adjustment did not affect the coupling-related influence on the variability of each climate mode, as confirmed by additional sensitivity simulations. Only the last 1000 years of each ensemble were used in the analysis.

Indices

The ENSO index was based on the Niño3.4 index, which indicates the average SSTA over the tropical PO (170°W, –120°W; 5°S, –5°N). The IOD index was defined as the difference in the SSTA between the western tropical IO (50°E–70°E and 10°S–10°N) and southeastern tropical IO (90°E–110°E and 10°S–EQ), known as the dipole mode index⁶. The index for the IOB-M was defined as the area-weighted average of the SSTA of the western IO (WIO) and southeastern IO (EIO), where the SSTA variability was strongest in the IO (Supplementary Fig. 1a), with weights of 0.657 and 0.343 for WIO and EIO, respectively. The focus of this study was not to precisely determine the characteristics of the IOB, but to analyze its interaction with the ENSO. Therefore, using only the two regions with the highest variability—those that most directly interact with the ENSO—adequately represents the features of the IOB. The similarities and differences between the IOB-M and actual IOB mode are discussed in the Results section.

Variability and periodicity of climate modes

In this study, we investigated how the interaction between the IO and PO influences the characteristics of climate modes, particularly their variability and periodicity.

The variability of the ENSO, IOD, and IOB-M was quantified as the standard deviation of each index, and their periodicity was determined by the peak period in the power spectra of each index. Spectral analysis was performed using the Multi-Taper-Method.

Definition of ENSO, IOB, and IOD events

A positive (El Niño) or negative (La Niña) ENSO event is defined when the 3-month running average Niño3.4 index is at or above (El Niño) or below (La Niña) ± 0.5 °C for 5 consecutive overlapping months. IOB and IOD events are identified during the respective maturation seasons. IOB events are detected when the IOB index exceeds a threshold of ± 0.75 standard deviation during the MAM season. Similarly, IOD events are defined when the dipole mode index exceeds a threshold of ± 0.75 standard deviation in the SON season.

Definition of extreme ENSO events

An extreme El Niño event is defined as the Niño3.4 index that exceeds 2 °C during the mature season (December–January–February months), whereas a strong La Niña event occurs when the Niño3.4 index is lower than –1.5 °C.

Separation of IOB-M and IOD influences on the ENSO

To distinguish the respective influences of the IOB-M and IOD on the ENSO, we transformed the model equation using fitted parameters for each pole (T_w and T_e). The original Eq. (4) for T_p , which incorporates the indices for each pole, can be transformed as shown in Eq. (5):

$$\frac{dT_p}{dt} = a_{11} T_p + a_{12} h_p + b_1 T_p^2 + b_2 T_p h_p + c_{wip1} T_w + c_{eip1} T_e + \sigma_1 \xi_1 \quad (4)$$

$$\begin{aligned} \frac{dT_p}{dt} = & a_{11} T_p + a_{12} h_p + b_1 T_p^2 + b_2 T_p h_p + (c_{wip1} + c_{eip1})(\alpha T_w + \beta T_e) \\ & + (\beta c_{wip1} - \alpha c_{eip1})(T_w - T_e) + \sigma_1 \xi_1 \end{aligned} \quad (5)$$

This transformation separated the combined effects of the IOB-M and IOD by isolating their distinct contributions using T_w and T_e . We investigated each effect by decoupling or adjusting the coupling strength using Eq. (5). The same approach was applied to h_p .

Decadal changes in Indo-Pacific climate modes

To detect changes in coupling strength, we first computed the parameters of the XRO model using a 30-year moving window. We then simulated the ENSO, IOB, and IOD indices using the model in each window to obtain 1000 ensemble members with 5000 years each. In each window, we calculated the standard deviations of the simulated indices over the last 1000 years and used the ensemble mean to facilitate their comparison with observations.

Sensitivity experiments

To confirm the coupling effect of each ocean, we performed several sensitivity experiments.

To confirm the role of coupling, we performed “decoupled experiments”. To see the effect of the PO on the IO, we set $C_{PO \rightarrow IO}$ to zero, while keeping everything else the same as in the control experiments. In case of seeing the effect of the IO on the PO, $C_{IO \rightarrow PO}$ was set to zero. The difference between the control and decoupled experiments implies the effects of one-way interaction by a specific basin.

To determine the different statistics of the climate modes depending on the coupling strength, “changing coupling experiments” were performed. We multiplied each coupling coefficient by γ , which varied from 0 to 2. The coefficient γ represents the annual cycle strength of the coupling strength between the basins. If $\gamma = 0$, then this experiment is identical to a decoupled experiment; if $\gamma = 1$, then it is a control experiment. We considered only the annual cycle strength of coupling because the variation in climate mode properties was influenced more by the annual cycle variation than by its annual mean variation (not shown). By considering different coupling strengths, we can understand the decadal changes in climate modes related to changes in coupling strength.

Finally, to determine whether changes in coupling effects influenced the decadal variability of the climate modes, “fixed coupling experiments” were conducted. In these experiments, $C_{PO \rightarrow IO}$ and $C_{IO \rightarrow PO}$ remained constant over time and were applied as fitted parameters throughout the entire period (1958–2023). By comparing the reconstructed indices using time-varying coupling parameter changes with those from fixed coupling experiments, we assessed the impact of decadal changes in the coupling strength on the decadal variability of climate modes.

Decadal modulation of the coupling coefficients

To verify the decadal variation in the coupling strength, we calculated the parameters of the XRO model using a 30-year moving window, advancing by 1 year at a time. To evaluate the rate of change in coupling strength over time, we regressed the 12 monthly coupling parameters from each window onto the corresponding 12 monthly coupling parameters fitted over the entire period (1958–2023), with the y-intercept fixed at zero. The resulting regression coefficients represent how the coupling strength in each time window deviates proportionally from the overall coupling strength over the entire period.

Data availability

ORAS5 is available from <https://cds.climate.copernicus.eu/cdsapp#!/dataset/reanalysis-oras5?tab=form>.

Code availability

All codes used in the manuscript are available upon request from H. J. Park, hjpark1021@yonsei.ac.kr.

Received: 19 May 2025; Accepted: 25 August 2025;

Published online: 03 October 2025

References

- McPhaden, M. J., Zebiak, S. E. & Glantz, M. H. ENSO as an integrating concept in earth science. *Science* **314**, 1740–1745 (2006).
- Timmermann, A. et al. El Niño–Southern oscillation complexity. *Nature* **559**, 535–545 (2018).
- Chu, J.-E. et al. Future change of the Indian Ocean basin-wide and dipole modes in the CMIP5. *Clim. Dyn.* **43**, 535–551 (2014).
- Klein, S. A., Soden, B. J. & Lau, N.-C. Remote sea surface temperature variations during ENSO: Evidence for a tropical atmospheric bridge. *J. Clim.* **12**, 917–932 (1999).
- Yang, J., Liu, Q., Xie, S.-P., Liu, Z. & Wu, L. Impact of the Indian Ocean SST basin mode on the Asian summer monsoon. *Geophys. Res. Lett.* **34**, L02708 (2007).
- Saji, N. H., Goswami, B. N., Vinayachandran, P. N. & Yamagata, T. A dipole mode in the tropical Indian Ocean. *Nature* **401**, 360–363 (1999).
- Webster, P. J., Moore, A. M., Loschnigg, J. P. & Leben, R. R. Coupled ocean–atmosphere dynamics in the Indian Ocean during 1997–98. *Nature* **401**, 356–360 (1999).
- Ha, K.-J., Chu, J.-E., Lee, J.-Y. & Yun, K.-S. Interbasin coupling between the tropical Indian and Pacific Ocean on interannual timescale: observation and CMIP5 reproduction. *Clim. Dyn.* **48**, 459–475 (2017).
- Ashok, K., Guan, Z. & Yamagata, T. Impact of the Indian Ocean dipole on the relationship between the Indian monsoon rainfall and ENSO. *Geophys. Res. Lett.* **28**, 4499–4502 (2001).
- Black, E., Slingo, J. & Sperber, K. R. An observational study of the relationship between excessively strong short rains in Coastal East Africa and Indian Ocean SST. *Mon. Wea. Rev.* **131**, 74–94 (2003).
- Clark, C. O., Webster, P. J. & Cole, J. E. Interdecadal variability of the relationship between the Indian Ocean Zonal Mode and East African Coastal Rainfall Anomalies. *J. Climate* **16**, 548–554 (2003).
- Zubair, L., Rao, S. A. & Yamagata, T. Modulation of Sri Lankan Maha rainfall by the Indian Ocean Dipole. *Geophys. Res. Lett.* **30**, 1063 (2003).
- Saji, N. H. & Yamagata, T. Structure of SST and Surface Wind Variability during Indian Ocean Dipole Mode Events: COADS Observations. *J. Climate* **16**, 2735–2751 (2003).
- Kug, J.-S. & Kang, I.-S. Interactive Feedback between ENSO and the Indian Ocean. <https://doi.org/10.1175/JCLI3660.1> (2006).
- Fischer, A. S., Terray, P., Guilyardi, E., Gualdi, S. & Delecluse, P. Two Independent Triggers for the Indian Ocean Dipole/Zonal Mode in a Coupled GCM. <https://doi.org/10.1175/JCLI3478.1> (2005).
- Alexander, M. A. et al. The Atmospheric Bridge: The Influence of ENSO Teleconnections on Air–Sea Interaction over the Global Oceans. (2002).
- Xie, S.-P. et al. Indian Ocean Capacitor Effect on Indo–Western Pacific Climate during the Summer following El Niño. <https://doi.org/10.1175/2008JCLI2544.1> (2009).
- Ashok, K., Behera, S. K., Rao, S. A., Weng, H. & Yamagata, T. El Niño Modoki and its possible teleconnection. *J. Geophys. Res. Oceans* **112**, C11007 (2007).
- Liu, Y., Cai, W., Lin, X., Li, Z. & Zhang, Y. Nonlinear El Niño impacts on the global economy under climate change. *Nat. Commun.* **14**, 5887 (2023).
- Cai, W. et al. Nonlinear country-heterogenous impact of the Indian Ocean Dipole on global economies. *Nat. Commun.* **15**, 5009 (2024).
- An, S.-I. A dynamic link between the basin-scale and zonal modes in the Tropical Indian Ocean. *Theor. Appl. Climatol* **78**, 203–215 (2004).
- Kug, J. et al. Role of the ENSO–Indian Ocean coupling on ENSO variability in a coupled GCM. *Geophys. Res. Lett.* **33**, 2005GL024916 (2006).
- Park, H.-J. et al. Local feedback and ENSO govern decadal changes in variability and seasonal synchronization of the Indian Ocean Dipole. *Commun. Earth Environ.* **5**, 1–8 (2024).
- Stuecker, M. F. et al. Revisiting ENSO/Indian Ocean Dipole phase relationships. *Geophys. Res. Lett.* **44**, 2481–2492 (2017).
- Park, H.-J., An, S.-I., Park, J.-H., Yang, Y.-M. & Kim, S.-K. Sub-seasonal impact of El Niño–Southern Oscillation on development of the Indian Ocean Dipole. *Commun. Earth Environ.* **6**, 374 (2025).
- Annamalai, H., Xie, S. P., McCreary, J. P. & Murtugudde, R. Impact of indian ocean sea surface temperature on developing El Niño. <https://doi.org/10.1175/JCLI-3268.1> (2005).
- Cai, W. et al. Pantropical climate interactions. *Science* **363**, eaav4236 (2019).

28. Wang, C. Three-ocean interactions and climate variability: a review and perspective. *Clim. Dyn.* **53**, 5119–5136 (2019).
29. Du, Y., Xie, S.-P., Huang, G. & Hu, K. Role of Air–Sea Interaction in the Long Persistence of El Niño–Induced North Indian Ocean Warming. <https://doi.org/10.1175/2008JCLI2590.1> (2009).
30. Wu, R., Kirtman, B. P. & Krishnamurthy, V. An asymmetric mode of tropical Indian Ocean rainfall variability in boreal spring. *J. Geophys. Res.* **113**, D5104 (2008).
31. Yang, Y. et al. Seasonality and Predictability of the Indian Ocean Dipole Mode: ENSO Forcing and Internal Variability. <https://doi.org/10.1175/JCLI-D-15-0078.1> (2015).
32. Kosaka, Y., Xie, S.-P., Lau, N.-C. & Vecchi, G. A. Origin of seasonal predictability for summer climate over the Northwestern Pacific. *Proc. Natl Acad. Sci.* **110**, 7574–7579 (2013).
33. Wang, C.-Y., Xie, S.-P. & Kosaka, Y. Indo-western pacific climate variability: ENSO forcing and internal dynamics in a tropical pacific pacemaker simulation. *J. Clim.* **31**, 10123–10139 (2018).
34. Izumo, T. et al. Influence of the state of the Indian Ocean Dipole on the following year's El Niño. *Nat. Geosci.* **3**, 168–172 (2010).
35. Annamalai, H., Kida, S. & Hafner, J. Potential Impact of the Tropical Indian Ocean–Indonesian Seas on El Niño Characteristics. <https://doi.org/10.1175/2010JCLI3396.1> (2010).
36. Luo, J.-J. et al. Interaction between El Niño and Extreme Indian Ocean Dipole. *J. Clim.* **23**, 726–742 (2010).
37. Fan, H., Wang, C., Yang, S. & Zhang, G. Coupling is key for the tropical Indian and Atlantic oceans to boost super El Niño. *Sci. Adv.* **10**, eadp2281 (2024).
38. Jansen, M. F., Dommenges, D. & Keenlyside, N. Tropical atmosphere–ocean interactions in a conceptual framework. <https://doi.org/10.1175/2008JCLI2243.1> (2009).
39. Dommenges, D., Semenov, V. & Latif, M. Impacts of the tropical Indian and Atlantic Oceans on ENSO. *Geophys. Res. Lett.* **33**, L11701 (2006).
40. Zhao, S. et al. Explainable El Niño predictability from climate mode interactions. *Nature* **630**, 891–898 (2024).
41. Wu, J. et al. Boosting effect of strong western pole of the Indian Ocean Dipole on the decay of El Niño events. *Npj Clim. Atmos. Sci.* **7**, 6 (2024).
42. Misra, V. The Teleconnection between the Western Indian and the Western Pacific Oceans. *Mon. Wea. Rev.* **132**, 445–455 (2004).
43. Ohba, M. & Ueda, H. An impact of SST anomalies in the indian ocean in acceleration of the El Niño to La Niña transition. *気象集誌 第2輯* **85**, 335–348 (2007).
44. Dayan, H., Izumo, T., Vialard, J., Lengaigne, M. & Masson, S. Do regions outside the tropical Pacific influence ENSO through atmospheric teleconnections? *Clim. Dyn.* **45**, 583–601 (2015).
45. Wu, R. & Kirtman, B. P. Understanding the Impacts of the Indian Ocean on ENSO Variability in a Coupled GCM. *J. Climate* **17**, 4019–4031 (2004).
46. Zhao, Y., Song, F., Sun, D., Dong, L. & Capotondi, A. Different roles of Indian Ocean Basin and Dipole modes in tropical Pacific climate variability. *Npj Clim. Atmos. Sci.* **8**, 1–11 (2025).
47. Okumura, Y. M. & Deser, C. Asymmetry in the Duration of El Niño and La Niña. <https://doi.org/10.1175/2010JCLI3592.1> (2010).
48. Crespo, L. R., Belén Rodríguez-Fonseca, M., Polo, I., Keenlyside, N. & Dommenges, D. Multidecadal variability of ENSO in a recharge oscillator framework. *Environ. Res. Lett.* **17**, 074008 (2022).
49. Sun, S., Fang, Y., Zu, Y., Liu, L. & Li, K. Increased occurrences of early Indian Ocean Dipole under global warming. *Sci. Adv.* **8**, eadd6025 (2022).
50. Abram, N. J., Gagan, M. K., Cole, J. E., Hantoro, W. S. & Mudelsee, M. Recent intensification of tropical climate variability in the Indian Ocean. *Nat. Geosci.* **1**, 849–853 (2008).
51. Ashok, K., Chan, W.-L., Motoi, T. & Yamagata, T. Decadal variability of the Indian Ocean dipole. *Geophys. Res. Lett.* **31**, L24207 (2004).
52. Tozuka, T., Luo, J.-J., Masson, S. & Yamagata, T. Decadal modulations of the indian ocean dipole in the SINTEX-F1 coupled GCM. *J. Clim.* **20**, 2881–2894 (2007).
53. Li, J. et al. El Niño modulations over the past seven centuries. *Nat. Clim. Change* **3**, 822–826 (2013).
54. El Niño modulations over the past seven centuries | Nature Climate Change. <https://www.nature.com/articles/nclimate1936>.
55. An, S.-I. & Wang, B. Interdecadal Change of the Structure of the ENSO Mode and Its Impact on the ENSO Frequency. *J. Climate* **13**, 2044–2055 (2000).
56. Chowdary, J. S. et al. Interdecadal Variations in ENSO Teleconnection to the Indo–Western Pacific for 1870–2007. <https://doi.org/10.1175/JCLI-D-11-00070.1> (2012).
57. Liu, F., Zhang, W., Jin, F.-F. & Hu, S. Decadal modulation of the ENSO–indian ocean basin warming relationship during the decaying summer by the interdecadal pacific oscillation. *J. Clim.* **34**, 2685–2699 (2021).
58. Xue, J., Luo, J., Zhang, W. & Yamagata, T. ENSO–IOD inter-basin connection is controlled by the atlantic multidecadal oscillation. *Geophys. Res. Lett.* **49**, e2022GL101571 (2022).
59. Peng, Q., Xie, S.-P. & Deser, C. Collapsed upwelling projected to weaken ENSO under sustained warming beyond the twenty-first century. *Nat. Clim. Change* **14**, 815–822 (2024).
60. Jiang, F., Seager, R. & Cane, M. A. A climate change signal in the tropical Pacific emerges from decadal variability. *Nat. Commun.* **15**, 8291 (2024).
61. Jin, F.-F. An equatorial ocean recharge paradigm for ENSO. Part I: Conceptual Model. *J. Atmos. Sci.* **54**, 811–829 (1997).
62. Jin, F.-F. et al. Simple ENSO models. in *El Niño Southern Oscillation in a Changing Climate* 119–151 (American Geophysical Union (AGU), <https://doi.org/10.1002/9781119548164.ch6> (2020).
63. Kim, S.-K. & An, S.-I. Untangling El Niño–La Niña asymmetries using a nonlinear coupled dynamic index. *Geophys. Res. Lett.* **47**, e2019GL085881 (2020).
64. Zuo, H., Balmaseda, M. A., Tietsche, S., Mogensen, K. & Mayer, M. The ECMWF operational ensemble reanalysis–analysis system for ocean and sea ice: a description of the system and assessment. *Ocean Sci.* **15**, 779–808 (2019).

Acknowledgements

This study was supported by the National Research Foundation of Korea (NRF) grants funded by the Korean government (MSIT) (RS-2023-00208000, NRF-2023R1A2C1004083) and the Yonsei Signature Research Cluster Program (2024-22-0162). S.I.A. was supported by a Yonsei Fellowship, funded by Lee Youn Jae.

Author contributions

S.I.A. conceived the original idea of the study. H.J.P. and S.I.A. initiated and conducted this study. H.J.P. performed the analyses and drafted the manuscript. All authors participated in discussions and contributed to the writing of the manuscript.

Competing interests

The authors declare no competing interests.

Additional information

Supplementary information The online version contains supplementary material available at <https://doi.org/10.1038/s41612-025-01217-3>.

Correspondence and requests for materials should be addressed to Soon-Il An.

Reprints and permissions information is available at <http://www.nature.com/reprints>

Publisher's note Springer Nature remains neutral with regard to jurisdictional claims in published maps and institutional affiliations.

Open Access This article is licensed under a Creative Commons Attribution-NonCommercial-NoDerivatives 4.0 International License, which permits any non-commercial use, sharing, distribution and reproduction in any medium or format, as long as you give appropriate credit to the original author(s) and the source, provide a link to the Creative Commons licence, and indicate if you modified the licensed material. You do not have permission under this licence to share adapted material derived from this article or parts of it. The images or other third party material in this article are included in the article's Creative Commons licence, unless indicated otherwise in a credit line to the material. If material is not included in the article's Creative Commons licence and your intended use is not permitted by statutory regulation or exceeds the permitted use, you will need to obtain permission directly from the copyright holder. To view a copy of this licence, visit <http://creativecommons.org/licenses/by-nc-nd/4.0/>.

© The Author(s) 2025